CrossMark

Melt Pool Analysis and Mesoscale Simulation of Laser Powder Bed Fusion Process (L-PBF) with Ti-6Al-4V Powder Particles

SANTOSH K. RAUNIYAR[1,2] and KEVIN CHOU[1]

1.—Department of Industrial Engineering, University of Louisville, Louisville, KY 40292, USA.
2.—e-mail: santosh.rauniyar@louisville.edu

The laser powder bed fusion (L-PBF) process is accompanied by rapid melting and solidification that results in intense thermocapillary convection within the melt pool. Open-source particle simulation software was utilized to generate a single layer of spherical powder particles of variable diameter. Considering the importance of particle size and the particle size distribution (PSD) in the L-PBF process, three distinct categories of PSD were generated with identical settings. A three-dimensional (3D) thermofluid model was developed in this study, incorporating the generated layer of powder particles of nonuniform size over a thick substrate. A moving volumetric heat source was applied to melt a single track in the powder layer using a user-defined function in FLUENT software. Temperature-dependent material properties including variable surface tension were considered in the computation. The numerical model was used to simulate Ti-6Al-4V powder particles to observe the melt pool flow dynamics. Presence of particles of smaller diameter in the powder mix supported consistent and continuous melt pool flow, while any kind of void enhanced fluid convection in the downward direction, causing a temporal increase in melt pool depth.

INTRODUCTION

Additive manufacturing (AM) has come a long way, transforming from a rapid prototyping to rapid manufacturing technology. It is anticipated that it will become a multibillion-dollar industry by the next decade.[1] The L-PBF process, one of the AM techniques, is quickly becoming one of the sought-after processes in aerospace and biomedical industries. Interest in and research work using this technique have grown exponentially over the past few years. In particular, additive manufacturing technologies for metal have found their way into various sectors with applications in cooling and automotive parts, medical implants, and aerospace components. Various commercial metallic powders including Ti6Al4V, In718, AlSi10Mg, and 304 and 316L stainless steels are being produced and modified specifically for this process. However, new powder materials must undergo calibration tests before application, which is both costly and time consuming.[2] Such calibration is required to determine the optimal processing parameters considering the thermal properties of each material.[3]

Modeling and simulation is an efficient substitute for experimental investigation, allowing understanding of the effect of process parameters on the L-PBF process. Use of numerical models to replicate the process provides enhanced understanding of the physical phenomena involved in such manufacturing techniques without actually producing any parts. Numerical models for laser–material interactions have been developed for laser beam welding since the 1980s.[4] Similar numerical methods have been utilized by researchers for the powder bed fusion process too. Although the physics of the L-PBF process is similar to that of the laser beam welding process, the presence of powder particles adds significant complexity to the process.[5]. Powder particles of different sizes also exhibit different absorbance properties. A Gaussian laser heat source has been used to model the L-PBF process,[6] although Khairallah et al.[7] used a laser ray-tracing method to model the heat source with greater accuracy. The randomness in the local distribution of particle sizes affects the heat transfer as well as the melt pool flow. The discrete element method (DEM) can be used to represent this distribution of

powder particles with greater accuracy.[8] Furthermore, spreading the next layer of particles affects the bonding between two layers and the overall density of the part.

Due to the complexity of the L-PBF process, it is not possible to replicate the mutliphysics phenomena using a single numerical model. Different models and techniques are thus applied separately to study the process on macro ($> 10^{-3}$ m), meso (10^{-6}–10^{-3} m), and microscale (10^{-9}–10^{-6} m). Some of the phenomena in the L-PBF process that have been simulated include the powder distribution, residual stresses, the temperature distribution, the melt pool flow, the effect of gas flow, and the microstructure. In the numerical model applied here, a mesoscale approach with mesh size of 5 μm was used to simulate the thermal interaction and melt pool flow. Experimental work on the effect of the PSD on optimization of the process parameters was reported by Liu et al.,[9] and Spierings et al.[10] compared the density of stainless steel 316L parts produced using different powder grades. Those studies showed that the PSD affects not only the flowability of the powder but also the density and surface finish of the final part.

In simple terms, the L-PBF process consists of repeated movement of a heat source over a metallic powder with diameter on the order of 10 μm, using various scanning patterns. Previous studies considered a single scan track to be representative of the process, to understand the process physics and melt pool flow dynamics.[7,11] The same approach is applied here, using a model consisting of a layer of metallic powder over a thick substrate. The DEM method is used to generate a layer of spherical powders with thickness of 60 μm. Powder particles with PSD from 0 μm to 25 μm, 0 μm to 45 μm, and 15 μm to 45 μm were generated with identical parameters. The powder and substrate material are both Ti-6Al-4V.

NUMERICAL MODELING

### Powder Distribution Modeling

A 3D model with domain size of 2500 μm $\times$ 600 μm $\times$ 1000 μm was created to obtain a random powder distribution representative of the powder bed on the build plate of a metal 3D printing machine. The powder size range shown in Fig. 1 is referenced from AP&C, A GE additive company's brochure. Powder particles with 15 different particle diameters were created in each of the three size ranges based on their proportions. A sequential powder addition algorithm was used to drop a constant number of particles in bulk into the domain as shown in Fig. 2, which were then allowed to settle under gravity.

Once the particles had settled, the bottom platform (collector) will move up and the recoater will spread the particles in the positive X-direction, as shown in Fig. 3. The result for the three different powder size distributions is quite different. The powder with size range of 0–25 μm shows comparatively less void space because the particles of smaller diameter fill in the void space, as shown in Fig. 4. The particles with size range of 0–45 μm and 15–45 μm showed a similar distribution of powder particles, but with more void space in between the particles.

Equations for Heat Transfer and Fluid Flow

A conical volumetric heat source was modeled, as given in Eq. 1, to represent the heat energy from the laser. It is important to identify the free surface in the mesh-based simulation to apply the appropriate volumetric heat source. Since there are two phases in the model, viz. gas as phase 1 and Ti-6Al-4V as phase 2, the free surface was tracked after each iteration using an UDF in FLUENT, before applying the heat energy for the next iteration. The volume of fluid equation used to track the free surface during melting and solidification is given in Eq. 2, where α represents the volume fraction

(a) Particle size distribution for Ti-6Al-4V particles	(b)		
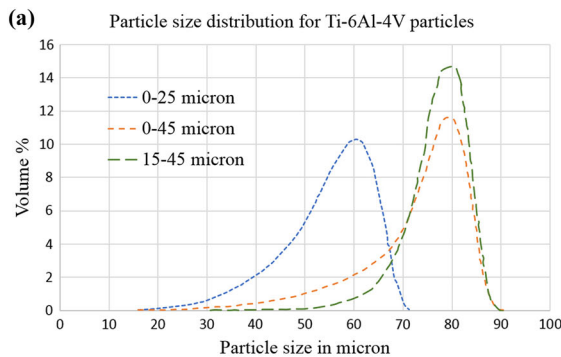
Size range	0-25 μm	0-45 μm	15-45 μm
Morphology	Spherical	Spherical	Spherical
Size distribution	μm	μm	μm
d10	8	14	20
d50	15	32	34
d90	24	47	46

Fig. 1. Particle size distribution for different categories: (a) graphical representation and (b) tabular data (adapted from Ref.[12]).
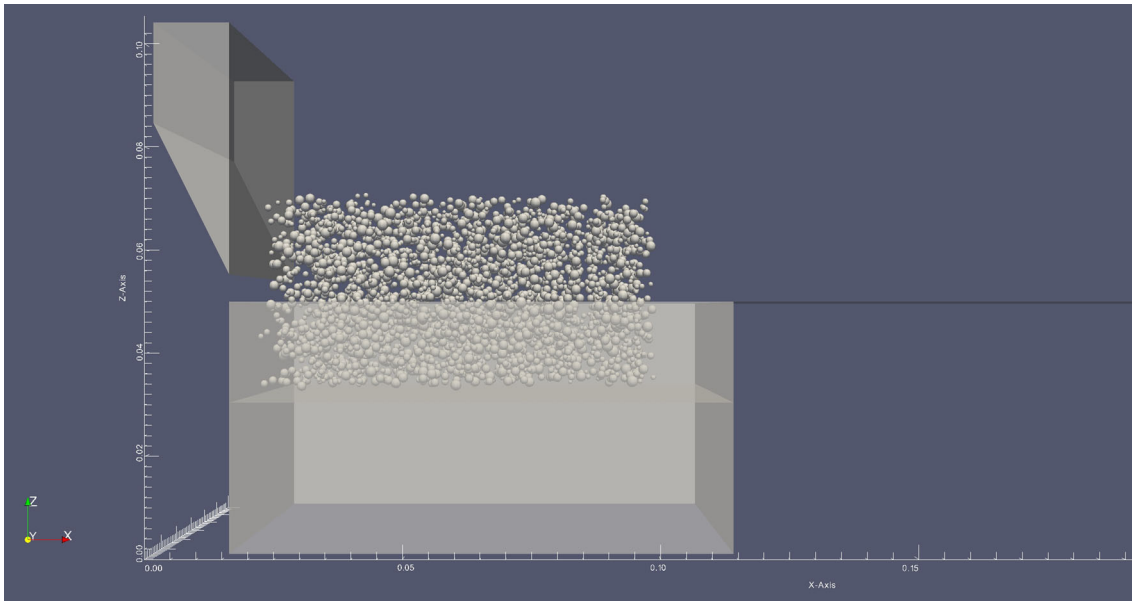
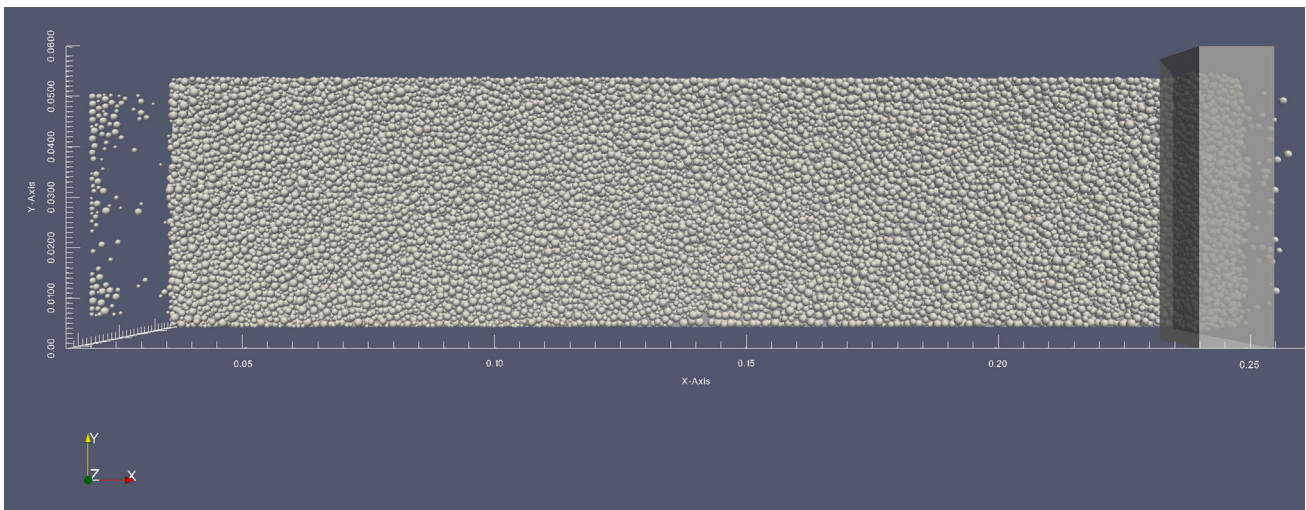Fig. 2. Side view of particle addition in bulk.

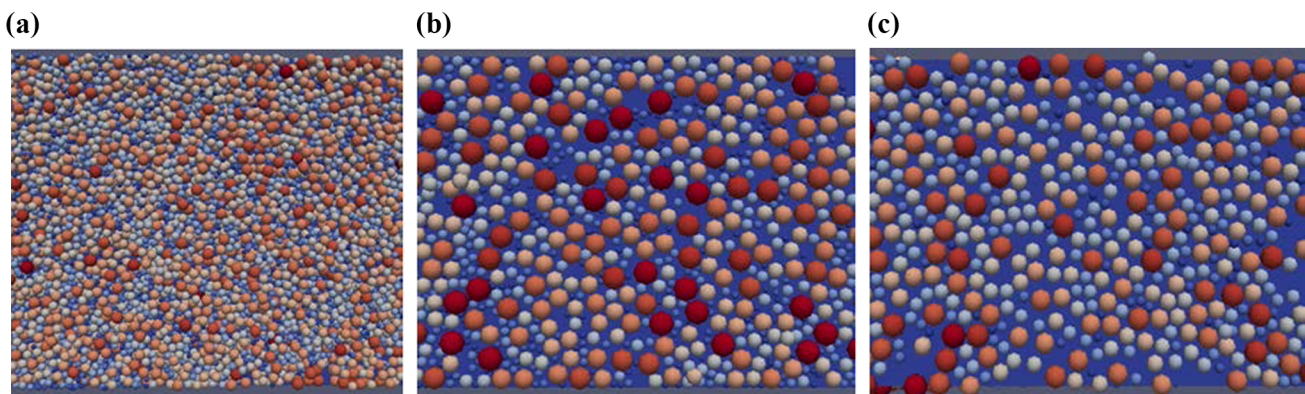Fig. 3. Top view of the domain with the powder spread.

(a)   **(b)**   **(c)**

Fig. 4. Zoomed view of generated powder layer for size range of (a) 0–25 μm, (b) 0–45 μm, and (c) 15–45 μm.
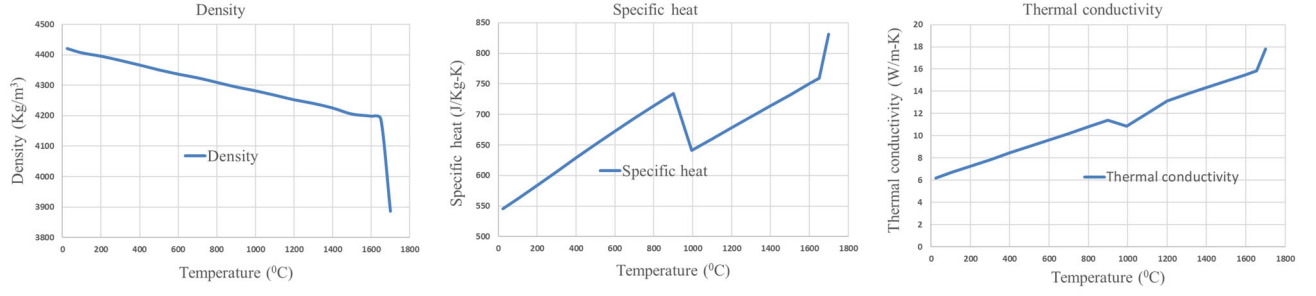
Fig. 5. Temperature-dependent material properties of Ti-6Al-4V.[13,14]

of fluid in a cell where $0 < \alpha < 1$. In each control volume, the volume fractions of all phases sum to unity.

$$\dot{Q}_{(x,y,z)} = \eta \times \frac{H_s \times I_z}{S}$$

$$I_z = \frac{1}{0.75}\left(-2.25\left(\frac{z}{S}\right)^2 + 1.5\left(\frac{z}{S}\right) + 0.75\right)$$

$$H_s = \frac{2P}{\pi d^2}\exp\left\{-\frac{2\left[(X-X_s)^2 + (Y-Y_s)^2\right]}{d^2}\right\}$$

(1)

where η is the absorption efficiency, P is the laser power, S is the penetration depth, d is the beam diameter, and X_S and Y_S define the position of the center of the heat source. H_s is the horizontal Gaussian distribution for the heat source, and I_z describes the decay of the magnitude of the heat source magnitude in the vertical direction.

$$\frac{\partial\alpha}{\partial t} + \vec{v}\cdot\nabla\alpha = 0$$

(2)

The boundary condition at the interface is given as

$$\frac{\partial(\rho H)}{\partial t} + \frac{\partial(\rho u_i H)}{\partial x_i} = \frac{\partial}{\partial x_i}\left(k\frac{\partial T}{\partial x_i}\right) + \dot{Q}(x,y,z)$$
$$- hA(T - T_\infty) - \sigma A\varepsilon\left(T^4 - T_\infty^4\right)$$

(3)

where H is the enthalpy, k is the thermal conductivity, $\dot{Q}_{(x,y,z)\text{int}}$ is the heat source applied at the interface, h is the heat transfer coefficient, σ is the Stefan–Boltzmann constant, ε is the emissivity used to account for the radiation through the top surface, and A is the free surface area of the cell. Adiabatic boundary conditions are applied on all walls of the domain.

The density, specific heat, and thermal conductivity are functions of temperature. These temperature-dependent material properties for Ti-6Al-4V were included in the model using piecewise-linear functions.[13] For liquid metal, a constant viscosity value was used. Also, a variable surface tension was included using a UDF, given by Eq. 4:

Table I. Material properties of Ti-6Al-4V and processing parameters

Parameter	Value
Solidus temperature, T_S (°C)	1605
Liquidus temperature, T_L (°C)	1655
Latent heat of fusion, L_f (kJ/kg)	440
Beam diameter, d (μm)	100
Power (W)	195
Scan speed (mm/s)	600
Viscosity(kg/m-s)	0.049
Ambient temperature (°C)	25
Emissivity, ε	0.5[15]
Stefan–Boltzmann constant, σ (kg s^{-3} K^{-4})	5.67×10^{-8}

$$\gamma = \gamma_m + \frac{d\gamma}{dT}\Delta T$$

(4)

where γ is the surface tension at a given temperature above the melting point, γ_m is the surface tension at the melting point, $\frac{d\gamma}{dT}$ is the surface tension gradient, and ΔT is the temperature difference between a given temperature and the melting temperature. In this study, the default value of the surface tension and surface tension gradient for Ti-6Al-4V resulted in strong depression of the melt pool, i.e., inadequate pull force. Therefore, both of these values were reduced by incorporating a factor into the UDF. The thermophysical properties of the material and the L-PBF processing parameters are presented in Fig. 5 and Table I. The default properties of argon gas preloaded in FLUENT were used for calculation of the model.

Thermofluid Modeling

The computational work was performed in a domain with size of 1200 μm × 400 μm × 250 μm. The powder particle coordinates along with their diameter data were imported from the result of the DEM simulation. The imported layer of powder particles with layer thickness of 60 μm lay on a 110-μm-thick substrate. A constant mesh size of 5 μm was used to generate a hexahedral mesh throughout the
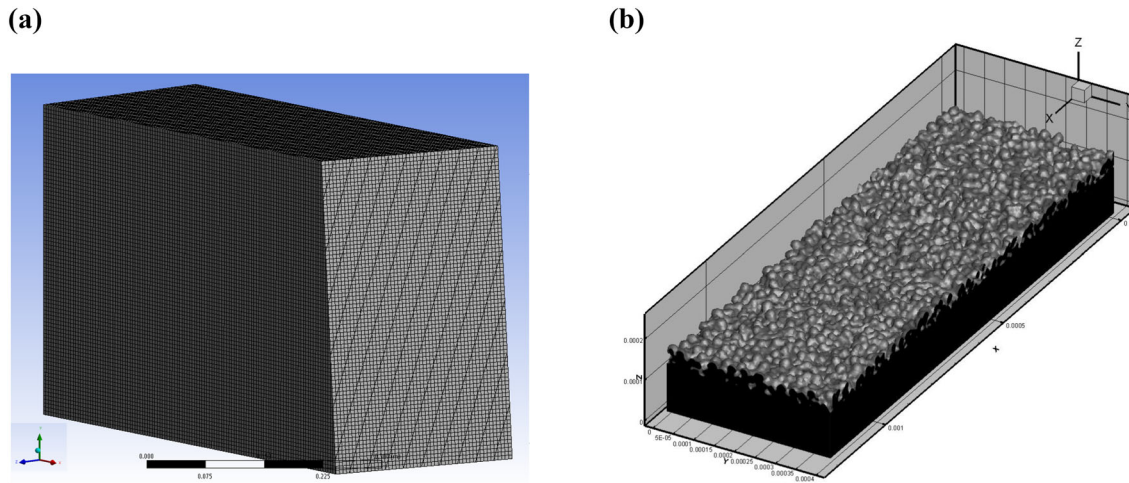
(a)

(b)

Fig. 6. (a) Meshed domain cross-section; (b) isometric view with cut section of model.

domain as shown in Fig. 6a. The total number of elements in the domain was approximately 1 million.

Figure 6b shows an isometric view of the model. Black color represents the thick substrate, while the grey color on top represents the powder particles. The rest of the domain is filled with argon gas. In this study, argon gas is considered as phase 1 and Ti-6Al-4V as phase 2. The free surface lies between the substrate and gas with volume fraction value ranging from 0 to 1.

RESULTS AND DISCUSSION

Melt Pool

The melt pool flow dynamics is described based on the result for the case using powder particles with size range of 0–25 μm with scan speed of 600 mm/s, power of 195 W, and laser absorption coefficient of 0.38. The results for two other cases and their comparison are discussed below. Application of the heat source (laser power) increases the temperature of a certain volume of powder. The material subject to the center portion of the incident laser beam will have the highest temperature, with a temperature gradient around it. Increase in the temperature melts the powder particle at the center, followed by melting of surrounding powder particles, as seen in Fig. 7a. Smaller powder particles in the mixture melt before larger powder particles. The melted powder fills the voids present between the powder particles due to the continuous flow of molten liquid, and the melt pool becomes dense. The melt pool then cools down and solidifies with the progress in time as the heat source moves from left to right. This process of melting and solidification continues, forming a single track. In case of high energy density, the temperature may exceed the boiling point of the material. This would result in evaporation and greater depression below the heat source. Such a scenario is not considered herein, and the effect of recoil pressure is also not included.

In the melting process, the flow of liquid metal is outwards, i.e., from higher to lower temperature, due to the surface tension gradient. As the heat source moves from left to right, the rear portion starts to cool due to thermal diffusion. During solidification, the melt flow changes direction from outer to inner, which contributes to the formation of a bead. This continuous process of melting and solidification leads to a continuous single track.

Figure 8 illustrates the transient behavior of the melt flow during single track formation, showing the volume fraction of fluid in a slice from a transverse cross-sectional view. The laser beam is the energy source and heats the powder at the center of the powder bed. The spherical powder slowly starts to change its shape at $t = 300$ μs. The melt pool depth keeps increasing until $t = 600$ μs. During solidification, the melt flow is pulled in the upward direction to form a track, as seen at $t = 900$ μs. The melt pool increases in depth during the heating period, then the flow reverses under the effect of increasing surface tension to form a solid track.

A single-track experiment was carried out using an EOS M270 machine with Ti-Al6-V4 powder with size distribution of 15–40 μm to quantitatively study the effect of the scan speed on the track width. The surface of the formed track was analyzed using white-light interferometry to obtain the melt pool width. Details of this study were presented in another publication.[16] The track width value obtained from this experiment followed the trend and was in good agreement with the computational result. At 600 mm/s, the width value from the experiment was 202.36 μm versus the simulation result of 200 $\pm$ 10 μm.

Comparison of the Results for Different Ranges of Powder Distribution

The powder with size distribution in the range of 0–25 μm showed comparatively less void space. The
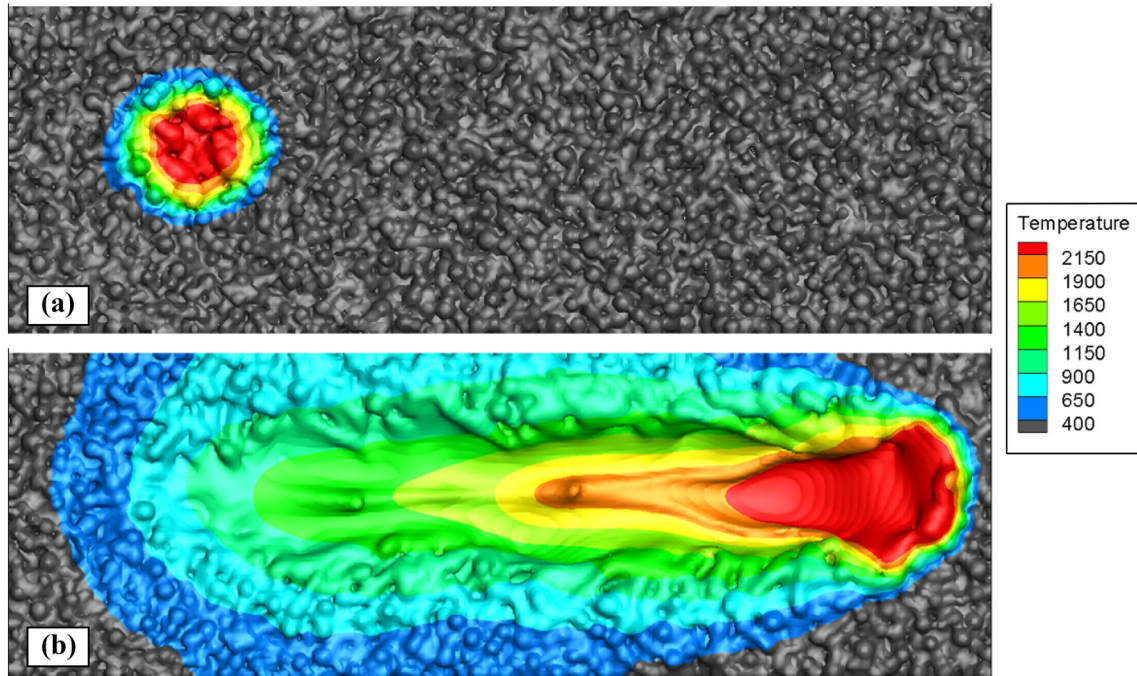
Fig. 7. Top view of powder bed showing (a) the melt pool at $t = 100$ μs and (b) the solidified track and melt pool at $t = 1500$ μs along with the temperature (°C) distribution.
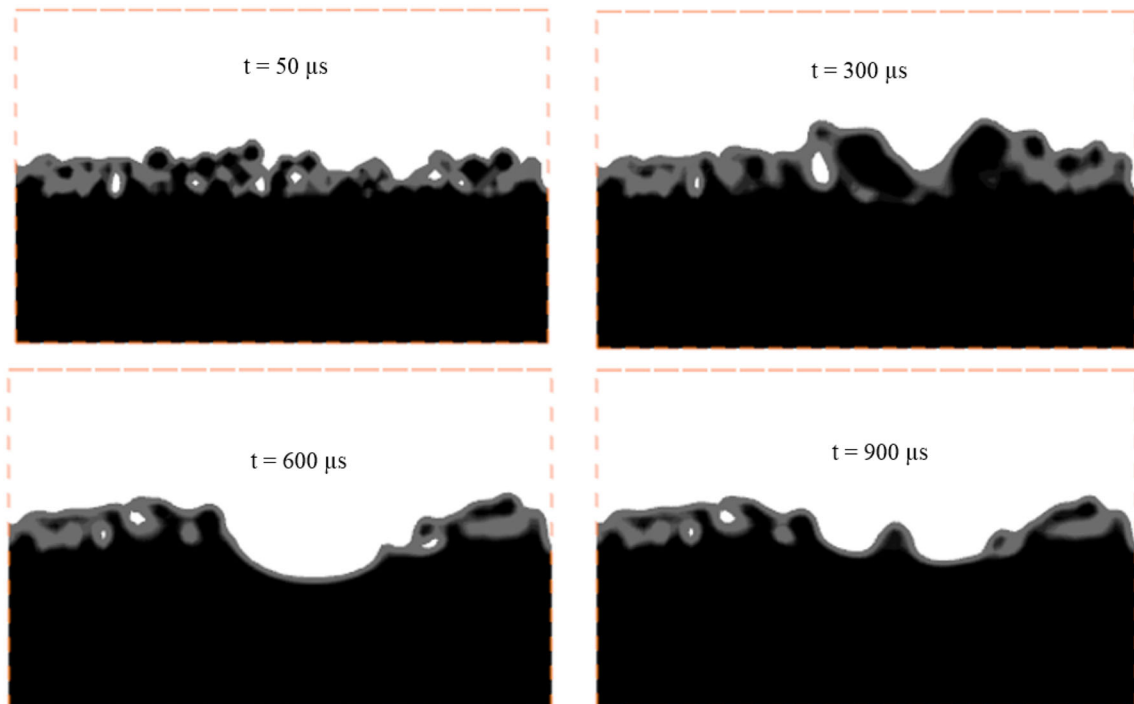

Fig. 8. Melt pool flow with time progression.

particles with smaller diameter filled the void space, whereas in the other two cases, there was more space between particles. Another factor affecting the void space is the lower and upper value of the

particle diameter, as is evident from the powder distribution results presented in Fig. 3. The size range of the powder simulated in this study showed that the lower value of particle diameter and lower
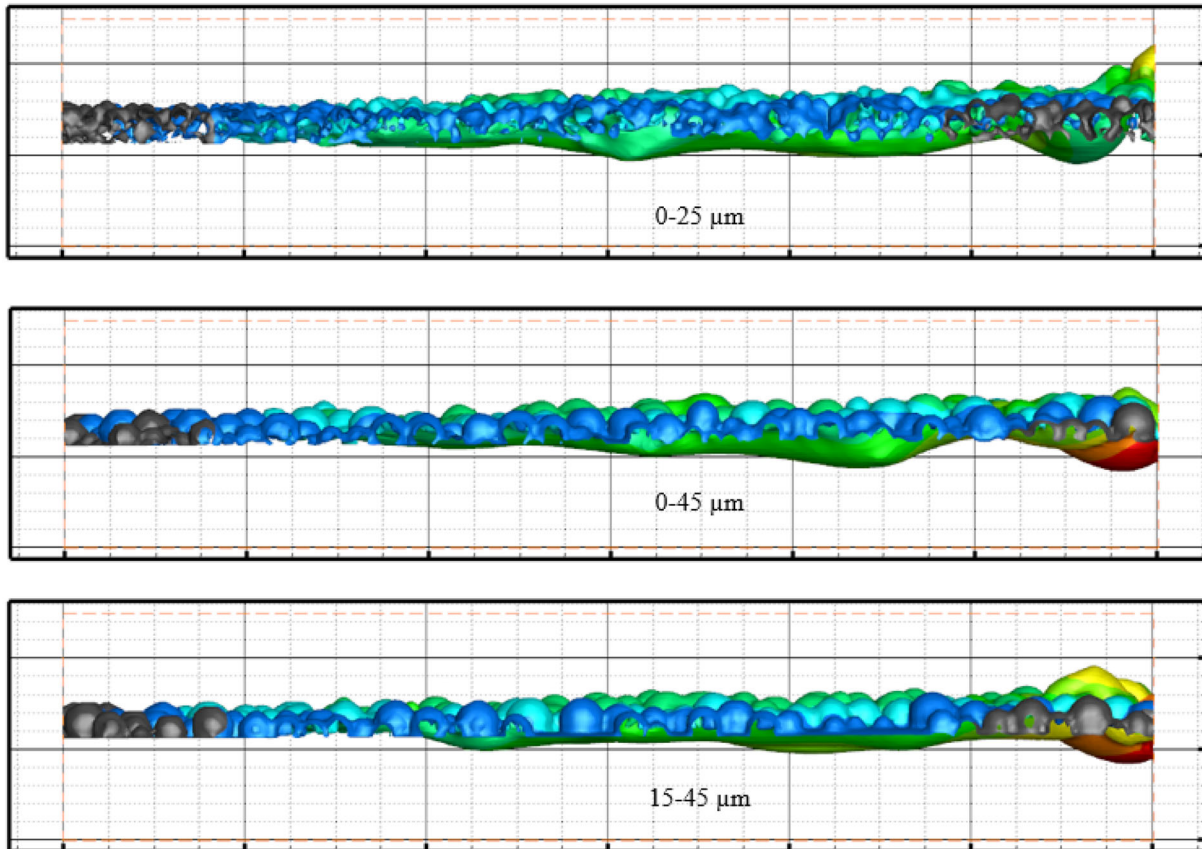
Fig. 9. Snapshot of temperature contour along with the solidified track at t = 2000 μs for three size ranges of powder distribution.

size range of the powder resulted in a more consistent and continuous melt pool flow, as shown in Fig. 9. For the same power, particles with larger diameter take more time to melt completely in comparison with those of smaller diameter. Thus, there is incompletely melted powder in the melt pool. The edges of the melt pool boundary also contain incompletely melted powder, giving rise to a coarser surface finish in the final part. Also, in the case of powder particles with larger diameter, the melt pool depth increases temporarily in the region where there are more large particles.

CONCLUSION

A DEM method was used to simulate powder particles of different size ranges and their distribution on a build plate. A 3D thermofluid model was developed and completed with the powder particle distribution and user-defined functions to model the heat source as well as to input other necessary parameters. The model was meshed at 5 μm to capture the melt pool flow dynamics at mesoscale level. Metallic powder with three size ranges was simulated under an identical condition to observe the effect of the powder distribution on the melt pool flow dynamics. The computational results lead to the following conclusions:

- The powder particle size and particle size distribution play an important role in the final part manufactured using the L-PBF process.
- Presence of particles of smaller diameter in the powder mix supports a consistent and continuous melt pool flow, while any kind of void enhances fluid convection in the downward direction, causing a temporal increase in melt pool depth.
- This model can be applied to predict the effect of key process parameters including the scan speed, power, and laser absorptivity on the melt pool dimensions.
- This study was carried out for power of 195 W and scan speed of 600 mm/s. Simulation results for powder distributions with different size ranges and different power intensities could also be analyzed for broader understanding.

One limitation of this model is that it assumes that all the powder particles are perfectly spherical, which is not the case for metal powders. Though no experimental work has been done during this study to validate the effect of the different ranges of powder particles, the model was successfully applied for quantitative analysis of the track width, applied for quantitative analysis of the track width for various scan speed at a constant power.

ACKNOWLEDGEMENT

REFERENCES

1. D.S. Thomas and S.W. Gilbert, *Costs and Cost Effectiveness of Additive Manufacturing*NIST Special Publication #1176, (Gaithersburg: NIST, 2014).
2. W.J. Sames, F.A. List, S. Pannala, R.R. Dehoff, and S.S. Babu, *Int. Mater. Rev.* 61, 315 (2016).
3. J.P. Kruth, G. Levy, F. Klocke, and T.H.C. Childs, *CIRP Ann. Manuf. Technol.* 56, 730 (2007).
4. S. Kou and Y.H. Wang, *Metal. Trans. A* 17, 2265 (1986).
5. Z. Lee, Mesoscopic simulation of heat transfer and fluid flow in laser powder bed additive manufacturing, in Proceedings of the Solid Freeform Fabrication Symposium, Austin, TX, p. 1154–1165 (2015).
6. P. Yuan and D. Gu, *J. Phys. D Appl. Phys.* 48, 035303 (2015).
7. S.A. Khairallah, A.T. Anderson, A. Rubenchik, and W.E. King, *Acta Mater.* 108, 36 (2016).
8. W.-H. Lee, Y. Zhang, and J. Zhang, *Powder Technol.* 315, 300 (2017).
9. B. Liu, R. Wildman, C. Tuck, I. Ashcroft, and R. Hague, Investigation the effect of particle size distribution on processing parameters optimisation in selective laser melting process, in Proceedings of the Solid Freeform Fabrication Symposium, Austin, TX, p. 227–238 (2011).
10. A.B. Spierings and G. Levy, Comparison of density of stainless steel 316L parts produced with selective laser melting using different powder grades, in Proceedings of the Solid Freeform Fabrication Symposium, Austin, TX, 342–353 (2009).
11. C. Panwisawas, B. Perumal, R.M. Ward, N. Turner, R.P. Turner, J.W. Brooks, and H.C. Basoalto, *Acta Mater.* 126, 251 (2017).
12. APC Brochure Montage (2018). http://advancedpowders.com/wp-content/uploads/APC_Brochure_Montage.pdf. Last accessed on 29 June 2018.
13. K.C. Mills (2002) *Aircr. Eng. Aerosp. Technol.* 74(5).
14. M. Boivineau, C. Cagran, D. Doytier, V. Eyraud, M.-H. Nadal, B. Wilthan, and G. Pottlacher, *Int. J. Thermophys.* 27, 507 (2006).
15. M. Kobayashi, M. Otsuki, H. Sakate, F. Sakuma, and A. Ono, *Int. J. Thermophys.* 20, 289 (1999).
16. S. Shrestha, S. Rauniyar, and K. Chou, *J. Mater. Eng. Perform.* (2018). https://doi.org/10.1007/s11665-018-3574-5.